Dark ice chemistry in interstellar clouds

Qasim, D.N.

Citation

Qasim, D. N. (2020, June 30). *Dark ice chemistry in interstellar clouds*. Retrieved from https://hdl.handle.net/1887/123114

Version:	Publisher's Version
License:	[Licence agreement concerning inclusion of doctoral thesis in the Institutional Repository of the University of Leiden](#)
Downloaded from:	[https://hdl.handle.net/1887/123114](#)

Note: To cite this publication please use the final published version (if applicable).

Cover Page

The handle http://hdl.handle.net/1887/123114 holds various files of this Leiden University dissertation.

Author: Qasim, D.
Title: Dark ice chemistry in interstellar clouds
Issue Date: 2020-06-30

Alcohols on the rocks: formed in a $H_3CC{\equiv}CH$ + OH cocktail

A number of recent experimental studies have shown that solid-state complex organic molecules (COMs) can form under conditions that are relevant to the CO freeze-out stage in dense clouds. In this work, we show that alcohols can be formed well before the CO freeze-out stage (i.e., during the very early stage of the H_2O-rich ice phase). This joint experimental and computational investigation shows that the isomers, n- and i-propanol ($H_3CCH_2CH_2OH$ and $H_3CCHOHCH_3$) and n- and i-propenol ($H_3CCH{=}CHOH$ and $H_3CCOH{=}CH_2$), can be formed in radical-addition reactions starting from propyne ($H_3CC{\equiv}CH$) + OH at the low temperature of 10 K, where $H_3CC{\equiv}CH$ is one of the simplest representatives of stable carbon chains already identified in the interstellar medium (ISM). The resulting average abundance ratio of 1:1 for n-propanol:i-propanol is aligned with the conclusions from the computational work that the geometric orientation of strongly interacting species is influential to the extent of which 'mechanism' is participating, and that an assortment of geometries leads to an averaged-out effect. Three isomers of propanediol are also tentatively identified in the experiments. It is also shown that propene and propane ($H_3CCH{=}CH_2$ and $H_3CCH_2CH_3$) are formed from the hydrogenation of $H_3CC{\equiv}CH$. This experimental finding falls in-line with the lower activation barrier of hydrogenation of a C=C bond in comparison to a C≡C bond. Reactants and products are probed by temperature programmed desorption-quadrupole mass spectrometry (TPD-QMS) and reflection-absorption infrared spectroscopy (RAIRS). Product relative abundances are determined from TPD-QMS data. Computationally-derived activation barriers give additional insight into what types of reactions and mechanisms are more likely to occur in the laboratory and in the ISM. Our findings not only suggest that the alcohols studied here share common chemical pathways and therefore can show up simultaneously in astronomical surveys, but also that their extended counterparts that derive from polyynes containing H_3C-$(C{\equiv}C)_n$-H structures may exist in the ISM. Such larger species, like fatty alcohols, are the possible constituents of simple lipids that primitive cell membranes on the early Earth are thought to be partially composed of.

8.1 Introduction

The origin of cosmic carbon lies in the outflows of carbon-rich stars (Cherch-neff 2011; Contreras & Salama 2013). How carbon evolves into hydrocarbon species, from small molecules such as methane (CH$_4$) and acetylene (C$_2$H$_2$) to polycyclic aromatic hydrocarbons (PAHs), to carbon nanoparticles, or other carbon containing species like alcohols, is far from understood. In addition to "bottom-up" approaches, which merges smaller precursors into larger species (in the gas-phase or solid-state), also "top-down" approaches have been proposed. Both scenarios are considered as likely road maps towards molecular complexity in space, but as mentioned, many details are lacking (Tielens 2013; Castellanos 2018).

From a bottom-up perspective, simple species such as C$_2$H$_2$ can polymerize to form polyacetylene ([C$_2$H$_2$]$_n$) (Woods et al. 2003; Cuylle et al. 2014). The complexity can increase by addition of a methyl (–CH$_3$) group to form methylpoly-acetylene. Such species can eventually accrete onto carbonaceous dust grains that were formed from nucleation of PAHs (Pascoli & Polleux 2000; Contreras & Salama 2013). An alternative is that these species form through surface reactions in the ice layers that are on top of dust grains. In this article, we focus on the simplest representative of the latter row of species: methylacetylene, also known as propyne (H$_3$CC≡CH). H$_3$CC≡CH has been detected in space (Snyder & Buhl 1973; Irvine et al. 1981; Kuiper et al. 1984; Cernicharo et al. 2001; Kaifu et al. 2004; Agúndez et al. 2008; Muller et al. 2011; Malek et al. 2011; Qiu et al. 2018). Not only is it reported to be observed towards carbon-rich stars (Agúndez et al. 2008) as expected, but it is also reported to be detected towards cold and dense clouds/cores (Kaifu et al. 2004; Irvine et al. 1981), where it has a column density of $(4-8) \times 10^{13}$ cm^{-2} in TMC-1 (Irvine et al. 1981). Assuming an H$_2$ abundance of $\sim 10^{21}$ cm^{-2} (Tielens 2013), this leads to $< 1\%$ with respect to H$_2$O ice following the calculation from Herbst & van Dishoeck (2009).

H$_2$O ice is formed on dust grains (Miyauchi et al. 2008; Ioppolo et al. 2008, 2010; Matar et al. 2008; Cuppen et al. 2010; Romanzin et al. 2011). Laboratory experiments show that every formed H$_2$O molecule, in the solid-state and gas-phase, has an OH radical and/or ion as an intermediate (van Dishoeck et al. 2013). In the ice, OH radicals have the chance to react with other species that are in direct proximity prior to hydrogenation to yield H$_2$O, as the accretion of an H-atom onto a dust grain of radius 10^{-5} cm happens once a day (Hama & Watanabe 2013). An example of this is the formation of CO$_2$ from CO and OH in H$_2$O-rich ices (Chang & Herbst 2012). Thus, the interaction between OH radicals and H$_3$CC≡CH is a valid topic to be addressed in astrochemical laboratories. This interaction may result in the formation of simple and polyalcohols.

The formation of alcohols is particularly intriguing as they may have a role in astrobiology, assuming that alcohols can be delivered to planetary bodies such as the early Earth (Chyba et al. 1990). Simple alcohols are amphiphilic molecules, i.e., both sides of the molecule have different affinities from each other (Moran et al. 2012). As they are composed of a polar head (–OH group) and a hydrophobic tale (aliphatic group), they can take part in the formation of micelles in primordial oceans. More complex alcohols (e.g., polyalcohols and

fatty alcohols), in turn, can play a role in the formation of primitive lipids. Like sugars in saccharolipids, sphingosines in sphingolipids, and glycerol in modern phospholipids, fatty alcohols can act as the backbone to which fatty acids are attached. Their presence during abiogenesis is supported by the idea that complex lipids may not have been available on the early Earth (Deamer et al. 2002; Budin & Szostak 2011), and also through the finding that primary alcohols are components of archaea cell membranes (De Rosa et al. 1986).

The mechanism proposed in this paper results in the formation of alcohols already in H_2O–rich ices. Meaning, the alcohols can be synthesized before the CO freeze-out stage, well below extinctions (A_V) of 9 in interstellar clouds (Boogert et al. 2015). In the literature, most solid-state laboratory experiments report the formation of simple alcohols (e.g., methanol (CH_3OH) and ethanol (H_3CCH_2OH)) and polyalcohols (e.g., ethylene glycol ($HOCH_2CH_2OH$), glycerol ($HOCH_2CHOHCH_2OH$), and methoxymethanol (H_3COCH_2OH)) in the context where much CO has already been frozen out (Bernstein et al. 1995; Chen et al. 2013; Abplanalp et al. 2016; Paardekooper et al. 2016; Fedoseev et al. 2015; Butscher et al. 2015; Chuang et al. 2016; Butscher et al. 2017). These experiments can be divided into two subgroups: 'energetic' and 'non-energetic' processing, where 'non-energetic' refers to a radical-induced process without the involvement of UV, cosmic rays, and/or other 'energetic' particles (Fuchs et al. 2009). In the 'energetic'-induced studies, CH_3OH and/or CO-containing ices are irradiated to form alcohols, and CH_3OH is either mixed with CO or explicitly stated to be a product of CO hydrogenation (Bernstein et al. 1995; Chen et al. 2013; Abplanalp et al. 2016; Paardekooper et al. 2016). In experiments that focus on 'non-energetic' processes, alcohols are formed by reactions that involve the hydrogenation of a CO-rich ice (Fedoseev et al. 2015; Butscher et al. 2015; Chuang et al. 2016; Butscher et al. 2017).

Many of the icy alcohols that have been formed in the laboratory have also been detected as gas-phase species in the ISM. This includes the detections of CH_3OH, H_3CCH_2OH, H_2CCHOH, $HOCH_2CH_2OH$, and H_3COCH_2OH, which were first reported by Ball et al. (1970), Zuckerman et al. (1975), Turner & Apponi (2001), Hollis et al. (2002), and McGuire et al. (2017), respectively. CH_3OH also has been detected in the solid-state (Boogert et al. 2011). Much effort has been recently put into explaining the transition from frozen to gas-phase CH_3OH to explain, for example, CH_3OH abundances observed in protoplanetary disks (van´t Hoff et al. 2018). Other alcohols are still elusive, such as n-propanol ($H_3CCH_2CH_2OH$) (Qasim et al. 2019).

This paper overviews the reaction of solid-state $H_3CC{\equiv}CH$ with H and OH under conditions relevant to the translucent cloud stage. Section 8.2 provides details on the experimental and computational parameters used for this study. Section 8.3 presents the findings from the laboratory experiments. Section 8.4 reports the computationally derived energies that are applicable to the reactions taking place in the experiments. These results are combined with the laboratory work to uncover the products formed and their formation pathways. Section 8.5 discusses how the formation of such icy alcohols can take place at the interface of astrochemical and astrobiological environments. Finally, the conclusions of this study are bulleted in Section 8.6.

Given the many different species that will be discussed in the next sections, Table 8.1 is added and summarizes the names and chemical structure formu-

Table 8.1: Chemical terminology used in this article.

IUPAC name	Referred to in this article
propan-1-ol (H$_3$CCH$_2$CH$_2$OH)	n-propanol
propen-1-ol (H$_3$CCH=CHOH)	n-propenol
propan-2-ol (H$_3$CCHOHCH$_3$)	i-propanol
propen-2-ol (H$_3$CCOH=CH$_2$)	i-propenol
propane-1,1-diol (H$_3$CCH$_2$CH(OH)$_2$)	propane-1,1-diol
propane-2,2-diol (H$_3$CC(OH)$_2$CH$_3$)	propane-2,2-diol
propane-1,2-diol (H$_3$CCHOHCH$_2$OH)	propane-1,2-diol
propan-2-one (H$_3$CCOCH$_3$)	acetone
propanal (H$_3$CCH$_2$CHO)	propanal
propanoic acid (H$_3$CCH$_2$COOH)	propanoic acid
propyne (H$_3$CC≡CH)	H$_3$CC≡CH
propene (H$_3$CCH=CH$_2$)	H$_3$CCH=CH$_2$
propane (H$_3$CCH$_2$CH$_3$)	H$_3$CCH$_2$CH$_3$

las of all relevant species. A majority of the listed chemicals are the expected products of solid-state H$_3$CC≡CH hydrogenation or hydroxylation.

8.2 Methodology

8.2.1 Experimental apparatus

The creation of ices and the subsequent measurements occur within an ultra-high vacuum (UHV) apparatus, SURFRESIDE^2. The main chamber reaches a base pressure of low 10^{-10} mbar. Near the center of the chamber, ices (typically tens of monolayers thick) are formed on a gold-plated copper substrate that is attached to a closed cycle helium cryostat. The inclusion of resistive heating and a sapphire rod allows the sample to have a temperature range of 7 - 450 K. The temperature is measured by a silicon diode sensor that has an absolute accuracy of 0.5 K. Further details of the initial design of SURFRESIDE^2 is found in Ioppolo et al. (2013), and recent upgrades are found in Qasim et al. (2018) and Chuang et al. (2018).

Two atomic beam lines are connected to the main chamber: a Hydrogen Atom Beam Source (HABS) and a Microwave Atom Source (MWAS). In this study, only the HABS is used, and more details about the design of the source is found in Tschersich & Von Bonin (1998), Tschersich (2000), and Tschersich et al. (2008). The HABS chamber is also under UHV conditions, where it reaches a base pressure of low 10^{-10} mbar. To form hydrogen atoms, hydrogen molecules (Linde 5.0) are thermally cracked by heated tungsten. This process also increases the kinetic energy of the H-atoms. To cool these atoms to room temperature, a nose-shaped quartz tube is positioned at the exit of the HABS source, which allows excess energy to be transferred via collisions with glass walls. Upon impact with

the icy surface, a fraction of the impinging H-atoms temporarily sticks to the ice that covers the surface and is thermalized. These H-atoms are then available for the reactions through the Langmuir-Hinshelwood mechanism. This mechanism was confirmed in several studies, where the intial step in the reaction chain initiated by H-atoms exhibits a significant activation barrier and requires quantum tunneling to proceed (Watanabe & Kouchi 2002; Watanabe et al. 2003; Cuppen & Herbst 2007; Fuchs et al. 2009; Chuang et al. 2016; Qasim et al. 2018).

All gases and vapors are prepared within a turbomolecularly-pumped gas manifold. $H_3CC\equiv CH$ (Sigma-Aldrich 97%), O_2 (Linde Gas 99.999%), and $^{18}O_2$ (Campro Scientific 97%) gases enter the main chamber through one of two dosing lines that are each connected to manually-operated leak valves. n-propanol (Honeywell 99.9%) and i-propanol (Sigma-Aldrich 99.8%) are placed in a tube and freeze-pump-thawed in order to rid of volatile impurities.

Two techniques are used to examine ice constituents and consequently the underlying ice chemistry: reflection-absorption infrared spectroscopy (RAIRS) and temperature programmed desorption quadrupole mass spectrometry (TPD-QMS). In this study, RAIRS is specifically exploited to identify the species formed at 10 K *in situ*. Spectra are recorded by a fourier transform infrared (FTIR) spectrometer that utilizes a wavenumber range of 4000-700 cm^{-1}, and can ultimately span to 6000 cm^{-1}. A resolution of 1 cm^{-1} is chosen. Vibrational mode assignments in the RAIR spectra originate from the NIST database.[1]

TPD-QMS is additionally utilized to probe newly formed ice species – particularly species that present a number of unresolved and/or overlapping infrared peaks. Employment of a QMS with an electron impact ionization energy of 70 eV allows comparison of the fragmentation (dissociative ionization) patterns from the experiments to fragmentation patterns found in the NIST database.[2] The relative abundances of $H_3CC\equiv CH$, $H_3CCH=CH_2$, and $H_3CCH_2CH_3$, as well as n- and i-propanol, are determined by a combination of the TPD-QMS data recorded at a molecule specific temperature and mass spectrometry data from NIST. The formula used to determine their relative abundances can be found in Martín-Doménech et al. (2015). $H_3CC\equiv CH$, $H_3CCH=CH_2$, and $H_3CCH_2CH_3$ have similar ionization cross sections of 7.66×10^{-16} cm^2, 8.74×10^{-16} cm^2, and 8.62×10^{-16} cm^2, respectively.[3] Additionally, the QMS sensitivity values of their correlating mass fragments, m/z = 43, m/z = 42, and m/z = 41, respectively, are similar. (Chuang 2018, Univ. Leiden) Therefore, only the fragmentation factors and relative intensities are taken into account, where the relative intensities are measured in the temperature range of 70 - 110 K. This method can also

1 T. Shimanouchi, "Molecular Vibrational Frequencies" in NIST Chemistry WebBook, NIST Standard Reference Database Number 69, Eds. P.J. Linstrom and W.G. Mallard, National Institute of Standards and Technology, Gaithersburg MD, 20899, https://doi.org/10.18434/T4D303, (retrieved December 4, 2018)
2 NIST Mass Spec Data Center, S.E. Stein, director, "Mass Spectra" in NIST Chemistry WebBook, NIST Standard Reference Database Number 69, Eds. P.J. Linstrom and W.G. Mallard, National Institute of Standards and Technology, Gaithersburg MD, 20899, https://doi.org/10.18434/T4D303, (retrieved December 4, 2018)
3 Kim, Y.-K., Irikura, K.K., Rudd, M.E., Ali, M.A., Stone, P.M., Chang, J., Coursey, J.S., Dragoset, R.A., Kishore, A.R., Olsen, K.J., Sansonetti, A.M., Wiersma, G.G., Zucker, D.S., and Zucker, M.A. (2004), Electron-Impact Ionization Cross Section for Ionization and Excitation Database (version 3.0). [Online] Available: http://physics.nist.gov/ionxsec [2019, March 16]. National Institute of Standards and Technology, Gaithersburg, MD.

be applied to determining the relative abundance of n- and i-propanol in the temperature range of 120 - 190 K, using m/z values of 31 for n-propanol, and 45 and 59 for i-propanol. However, their respective sensitivity values of 0.3179, 0.1762, and 0.0982 are taken into account, as their values will significantly influence the determined relative abundances. A TPD ramp rate of 5 K/min is applied to all experiments.

8.2.2 Experimental procedure

The experiments and experimental parameters used in this study are listed in Table 8.2. Fluxes are determined by the Hertz-Knudsen equation (Kolasinski 2012) except for the H-atom flux, which is based on an absolute D-atom flux measurement that is reported in Ioppolo et al. (2013). Motivation for the listed experiments is discussed below.

Experiments 1.0 - 1.2 are used to show what products are formed from the hydrogenation of $H_3CC{\equiv}CH$ ice, as well as to determine the relative abundance of the newly formed products. The addition of oxygen in experiments 2.0 - 2.3 is used to study the products formed from $H_3CC{\equiv}CH$ + OH and their subsequent relative abundance. Note that OH radicals are effectively formed from H + O_2 (Cuppen et al. 2010). $^{18}O_2$ is used in experiments 2.1 and 2.3 in order to confirm the identity of species formed in experiments 2.0 and 2.2, respectively, by observation of the isotopic shift in the TPD-QMS data. To further confirm the identity of the species formed in experiments 2.0 - 2.3, the TPD-QMS data of experiments 3.0 - 3.2 are used as references.

8.2.3 Computational details

We calculate activation energies and reaction energies for the reactions of hydrogen atoms and hydroxyl radicals with both $H_3CC{\equiv}CH$ and $H_3CCH{=}CH_2$ molecules. Benchmark calculations and additional supporting information are found in the Supporting Information Section S2. As radicals may attack either the center or exterior carbon atom, this results in a total of eight reactions. Additionally, two isomerization reactions are studied, namely the conversion from n-propenol to propanal (and vice versa) and i-propenol to acetone (and vice versa).

The potential energy surface (PES) or electronic structure is described by density functional theory (DFT). Following the benchmark calculations performed by Kobayashi et al. (2017), the MPWB1K functional (Zhao & Truhlar 2004) in combination with the basis set def2-TZVP (Weigend et al. 1998) is chosen. The energy and gradient calculations are carried out in NWChem version 6.6 (Valiev et al. 2010). An additional benchmark is performed for the activation energies with the M06-2X functional (Zhao & Truhlar 2008) with the same basis set (def2-TZVP). Furthermore, the interaction energies of the OH-C_3H_n pre-reactive complexes calculated with MPWB1K/def2-TZVP are compared to single-point energies calculated with CCSD(T)-F12/cc-VDZ-F12 (Knowles et al. 1993, 2000; Deegan & Knowles 1994; Adler et al. 2007; Peterson et al. 2008; Knizia et al. 2009) in Molpro version 2012 (Werner et al. 2012).

Geometry optimizations are carried out for the separated reactant, product, and transition structures and verified by the appropriate number of imaginary

Table 8.2: A list of experiments performed and the corresponding experimental parameters. Fluxes are calculated by the Hertz-Knudsen equation, and the H-flux is derived from Ioppolo et al. (2013). "Other" refers to either n- or i-propanol.

No.	Experiments	T_{sample} K	$Flux_{HC\equiv CCH_3}$ $cm^{-2}s^{-1}$	$Flux_H$ $cm^{-2}s^{-1}$	$Flux_{O_2}$ $cm^{-2}s^{-1}$	$Flux_{other}$ $cm^{-2}s^{-1}$	Time s
			$H_3CC\equiv CH$ hydrogenation				
1.0	$H_3CC\equiv CH$	10	2×10^{12}	-	-	-	21600
1.1	$H_3CC\equiv CH + H$	10	2×10^{12}	5×10^{12}	-	-	21600
1.2	$H_3CC\equiv CH + H$	10	7×10^{12}	5×10^{12}	-	-	7200
			$H_3CC\equiv CH$ and $O_2/^{18}O_2$ hydrogenation				
2.0	$H_3CC\equiv CH + H + O_2$	10	7×10^{12}	5×10^{12}	1×10^{12}	-	21600
2.1	$H_3CC\equiv CH + H + {}^{18}O_2$	10	7×10^{12}	5×10^{12}	1×10^{12}	-	21600
2.2	$H_3CC\equiv CH + H + O_2$	10	2×10^{12}	5×10^{12}	4×10^{12}	-	21600
2.3	$H_3CC\equiv CH + H + {}^{18}O_2$	10	2×10^{12}	5×10^{12}	4×10^{12}	-	21600
			Reference experiments				
3.0	n-propanol	10	-	-	-	3×10^{12}	3600
3.1	i-propanol	10	-	-	-	3×10^{12}	3600
3.2	i-propanol + H + O_2	10	-	5×10^{12}	1×10^{12}	2×10^{10}	7200
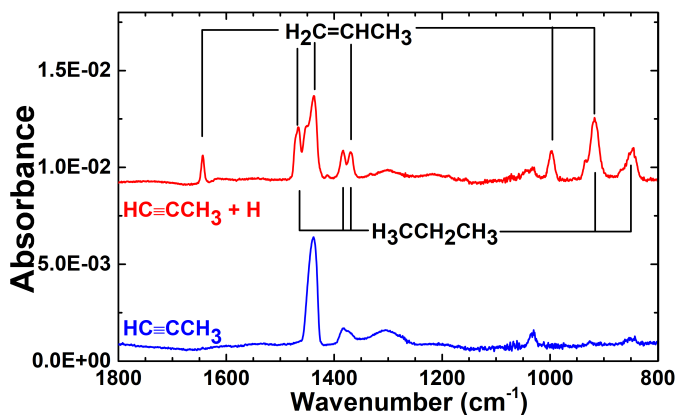
Figure 8.1: RAIR spectra acquired after deposition of $HC\equiv CCH_3$ (bottom spectrum; exp. 1.0) and $HC\equiv CCH_3$ + H (top spectrum; exp. 1.1) on a 10 K surface. The infrared peaks of newly formed $H_3CCH=CH_2$ and $H_3CCH_2CH_3$ are highlighted. RAIR spectra are offset for clarity.

frequencies. A transition structure is characterized by the Hessian bearing exactly one negative eigenvalue. To confirm that the found transition structure connects the desired reactant and product, an intrinsic reaction coordinate (IRC) search is conducted. From the end-point of the IRC, a re-optimization is performed to obtain the pre-reactive complex (PRC). All calculations are performed with DL-find (Kästner et al. 2009) within Chemshell (Sherwood et al. 2003; Metz et al. 2014). IRC searches are performed using the algorithm described by Meisner et al. (2017) and Hratchian & Schlegel (2004). Finally, for the reaction OH + $H_3CCH=CH_2$, transition states are only found through a nudged elastic band (NEB) approach.

All calculated energies include a zero-point energy (ZPE) correction that is listed separately. Note that these ZPE corrections can be quite sizable and are thus important to include due to their impact on the total activation energy. Finally, activation energies are calculated with respect to both separated reactants (SR) and the pre-reactive complex (PRC). Although the difference between these two approaches lies only in the considered starting point of the reaction, the effect on the activation energies again can be quite pronounced.

All calculations are performed in the gas-phase as we expect the influence of H_2O molecules in the neighborhood of unsaturated hydrocarbons to play a minor role in altering the reaction potential energy landscape (Kobayashi et al. 2017).

8.3 Experimental results and discussion

8.3.1 Hydrogenation of $HC\equiv CCH_3$

The formation of $H_3CCH=CH_2$ and $H_3CCH_2CH_3$ by the hydrogenation of $H_3CC\equiv CH$ at 10 K is visible from the RAIR data displayed in Figure 8.1 (upper panel), and

Table 8.3: The relevant normal vibrational modes detected in the $HC\equiv CCH_3$ + H (exp. 1.1) and $HC\equiv CCH_3$ + H + O_2 (exp. 2.0) experiments.

Peak position (cm^{-1})	Peak position (μm)	Molecule	Reference
851	11.75	$H_3CCH_2CH_3$	a, b
917	10.91	$H_3CCH=CH_2$ and $H_3CCH_2CH_3$	d; c, a, b
997	10.03	$H_3CCH=CH_2$	d
1030	9.71	$H_3CC\equiv CH$	this work
1370	7.30	$H_3CC\equiv CH$, $H_3CCH=CH_2$ and $H_3CCH_2CH_3$	this work; d; c, a, b
1384	7.23	$H_3CC\equiv CH$ and $H_3CCH_2CH_3$	this work; c, a, b
1439	6.95	$H_3CC\equiv CH$ and $H_3CCH=CH_2$	this work; d
1466	6.82	$H_3CCH=CH_2$ and $H_3CCH_2CH_3$	d; c, a, b
1644	6.08	$H_3CCH=CH_2$	d
1669	5.99	$H_3CCH=CHOH/H_3CCOH=CH_2$*	e

a(NIST) b(Comeford & Gould 1961) c(Ghosh et al. 2018) d(Abplanalp et al. 2018)
e(Shaw et al. 2017)
* indicates tentative identification

the corresponding vibrational mode assignments are listed in Table 8.3. Despite the overlap of a number of vibrational bands between $H_3CCH=CH_2$ and $H_3CCH_2CH_3$, there are distinct peaks that are characteristic to these species and also do not overlap with the IR signatures of $H_3CC\equiv CH$. The C=C stretch of $H_3CCH=CH_2$ at 1644 cm^{-1} (Abplanalp et al. 2018) is conveniently isolated, and the C-C stretch of $H_3CCH_2CH_3$ at 851 cm^{-1} is clearly visible. The hydrogenation of $H_3CC\equiv CH$ to form $H_3CCH=CH_2$ and $H_3CCH_2CH_3$ parallels the hydrogenation of the two-carbon counterpart, acetylene (HCCH), which results in the formation of ethene ($H_2C=CH_2$) and ethane (H_3CCH_3) (Kobayashi et al. 2017).

TPD-QMS spectra provide additional proof for the newly formed $H_3CCH=CH_2$ and $H_3CCH_2CH_3$ from $H_3CC\equiv CH$ hydrogenation, and are presented in Figure 8.2. The m/z fragment values upon 70 eV electron impact ionization with the highest relative intensities for $H_3CCH=CH_2$ and $H_3CCH_2CH_3$ are 41 and 29, respectively (NIST). The desorption peak temperature of $H_3CCH_2CH_3$ from an amorphous solid H_2O surface is ~ 80 K (Smith et al. 2015), a peak that is also observed in Figure 8.2. Since $H_3CCH_2CH_3$ is composed of single bonds and $H_3CCH=CH_2$ has a double bond, $H_3CCH_2CH_3$ should have a lower desorption energy than $H_3CCH=CH_2$ (an effect of pi stacking) (Nykänen & Honkala 2011). Thus, the desorption at 81 K is assigned as the main desorption peak of $H_3CCH_2CH_3$, and the higher temperature signal at 86 K must be the main desorption peak of $H_3CCH=CH_2$. Additionally, it is observed that some $H_3CCH_2CH_3$ co-desorbs with $H_3CCH=CH_2$ at 86 K, which maybe due to the amorphous to crystalline phase transition of $H_3CC\equiv CH$, since m/z = 29 is not a fragment value of $H_3CCH=CH_2$ (or $H_3CC\equiv CH$), yet there is a desorption peak for m/z = 29 at 86 K. The desorption of the bulk of unreacted $H_3CC\equiv CH$ ice peaks around 104 K.

The abundance of $H_3CCH_2CH_3$ is measured to be 2-3 times greater than that of $H_3CCH=CH_2$. This infers that the hydrogenation of $H_3CCH=CH_2$ to form $H_3CCH_2CH_3$ is faster than hydrogenation of $HC\equiv CCH_3$ to yield $H_3CCH=CH_2$.
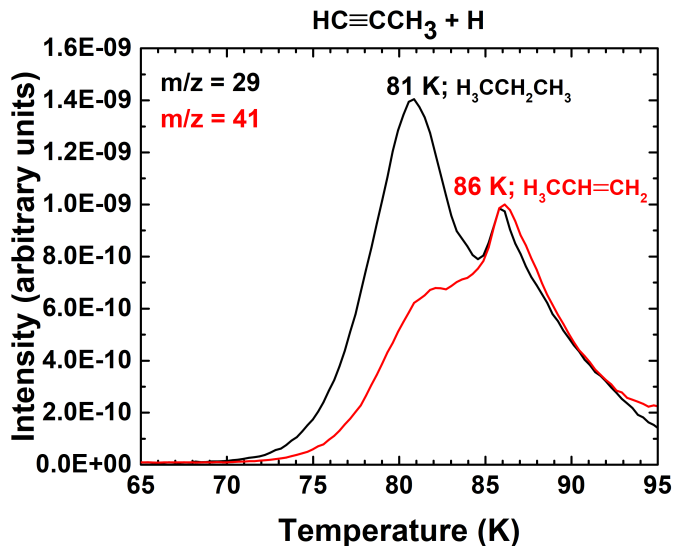
Figure 8.2: TPD-QMS fragment spectra acquired after deposition of HC≡CCH$_3$ + H (exp. 1.2) on a 10 K surface. The main desorption peaks of newly formed H$_3$CCH$_2$CH$_3$ and H$_3$CCH=CH$_2$ are shown at 81 and 86 K, respectively, by m/z = 29 (C$_2$H$_5^+$) and 41 (C$_3$H$_5^+$). A HC≡CCH$_3$:H$_3$CCH=CH$_2$:H$_3$CCH$_2$CH$_3$ abundance ratio of 9:1:2 is measured.

The work of Kobayashi et al. (2017) reported a similar result for the two-carbon equivalents, H$_2$C=CH$_2$ and H$_3$CCH$_3$, where the effective hydrogenation reaction rate constant was found to be ∼ 3 times higher for H$_3$CCH$_3$ than for H$_2$C=CH$_2$.

8.3.2 Inclusion of OH into HC≡CCH$_3$ hydrogenation network

8.3.2.1 Experimental evidence of n- and i-propanol formation

As shown in Figure 8.1, the number of overlapping bands makes it difficult to discern between the RAIR features of H$_3$CCH=CH$_2$ and H$_3$CCH$_2$CH$_3$, with only two distinct bands apparent. The RAIR spectra become even more convoluted when O$_2$ is added to the mixture. Figure 8.3 displays the RAIR spectrum of H$_3$CC≡CH + H + O$_2$, in addition to four control RAIR spectra, to attempt characterization of the infrared bands in exp. 2.0. Spectra of n- and i-propanol are compared as they are expected products from the H$_3$CC≡CH + H + O$_2$ experiment, and are also commercially available and feasible for UHV conditions. Comparison of the n- and i-propanol spectra to the HC≡CCH$_3$ + H spectrum shows that many of the RAIR features overlap with each other. Additionally, some bands that arise in the H$_3$CC≡CH + H + O$_2$ experiments are difficult to identify (asterisked in Figure 8.3) as expected, since the hydrogenation of a three-carbon species with O$_2$ is a relatively complex molecular reaction. Thus, the overlapping infrared signals belonging to identified and unidentified molecules make it complicated to track the formation of n- and i-propanol in

the infrared at 10 K or even in temperature-dependent RAIR spectra. As discussed in Ioppolo et al. (2014), the formation of complex organic molecules at low temperatures can alternatively be shown by TPD-QMS experiments.
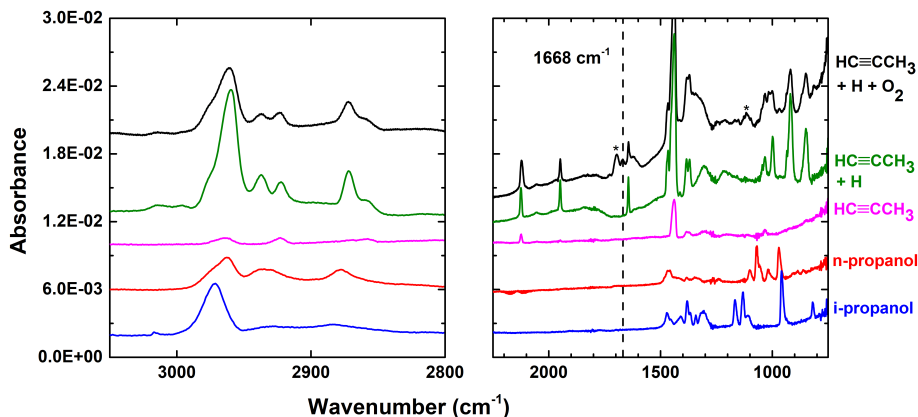
Figure 8.3: (Top to bottom) RAIR spectra acquired after deposition of HC≡CCH$_3$ + H + O$_2$ (exp. 2.0; column density of 1×10^{16} cm^{-2}), HC≡CCH$_3$ + H (exp. 1.1), HC≡CCH$_3$ (exp. 1.0), n-propanol (exp. 3.0; column density of 1×10^{16} cm^{-2}), and i-propanol (exp. 3.1; column density of 1×10^{16} cm^{-2}) on a 10 K surface. * indicates peaks that are unidentified, and the band highlighted with a dashed line in the top spectrum is likely due to n- or i-propenol. These are further discussed in Section 8.3.2.2. RAIR spectra are offset for clarity.

Figure 8.4 shows the desorption of newly formed n- and i-propanol (and their isotopic counterparts) in two different isotope experiments, where an average abundance ratio of 1:1 for n-propanol:i-propanol is measured. In the H$_3$CC≡CH + H + O$_2$ experiment, the m/z values with the highest intensities for n- and i-propanol are 31 and 45, respectively. Other fragments, such as m/z = 60 and 46, are also shown. In the H$_3$CC≡CH + H + ^{18}O$_2$ experiment, the m/z values bump up to 33 and 47, respectively, due to isotopically enhanced oxygen. The fragmentation patterns that represent the desorptions of n- and i-propanol are shown in Figure 8.5. For the desorption of n-propanol at 163 K, the measured relative intensities are 100:2 for m/z = 31:60, 100:3 for m/z = 33:62, and 100:2 for m/z = 31:60. Concerning the desorption of formed i-propanol at 160 K, the relative intensities are also consistent, with ratios of 100:3 for m/z = 45:46, 47:48, and 45:46. The consistency of the relative intensities found between the isotope experiments, and well as between the isotope experiments and the pure n- and i-propanol experiments, further supports the confirmation of solid-state formation of both propanols.

The desorption temperature acts as a further diagnostic, in that the desorption temperature of certain species can shift when they are trapped by relatively less volatile species (Collings et al. 2004). An example of this is demonstrated in the Supporting Information Figure S1, where the peak desorption of pure i-propanol is seen at 150 K, and shifts to 160 K upon addition of H and O$_2$, which
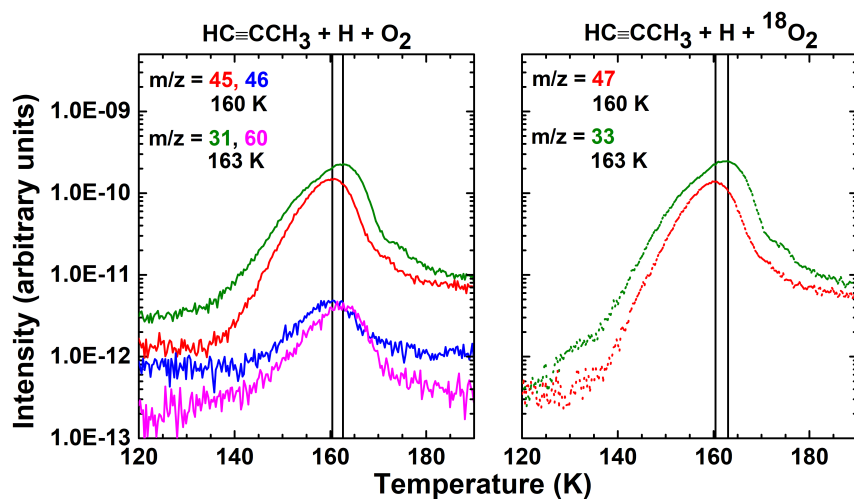
Figure 8.4: TPD-QMS fragment spectra acquired after deposition of $HC\equiv CCH_3$ + H + O_2 (left; exp. 2.0) and $HC\equiv CCH_3$ + H + $^{18}O_2$ (right; exp. 2.1) on a 10 K surface. The desorption peaks of newly formed i-propanol and n-propanol are shown at 160 and 163 K, respectively. An n-propanol:i-propanol average abundance ratio of 1:1 is measured.

is the desorption temperature observed for newly formed i-propanol shown in Figure 8.4.

8.3.2.2 Tentative experimental evidence of the formation of other oxygen-bearing COMs: n- and i-propenol

The $H_3CC\equiv CH$ + H + O_2 experiment is expected to generate a variety of COMs that unfortunately not only pushes the limits of the TPD-QMS technique in unambiguously distinguishing the different products formed, but also yields species that are not commercially available for control purposes or are challenging to use in a UHV setup. Example reaction products are n- and i-propenol, which are not commercially available as they undergo keto-enol tautomerism at room temperature to primarily form propanal and acetone, respectively (Shaw et al. 2017). However at lower temperatures, the enol form becomes more stabilized (Burdett & Rogers 1966), thus n- and i-propenol ices can be present under the applied experimental conditions following addition of OH to the triple bond of $H_3CC\equiv CH$. Tentative identifications in the RAIR and TPD-QMS data are discussed below. Note that although there is partial evidence for n- and i-propenol formation from the experimental data, the inclusion of computationally-derived results confirms their presence in the experiments, and is discussed in a later section.

The dashed line in Figure 8.3 shows the potential identification of n- or i-propenol marked at 1668 cm^{-1} in the $H_3CC\equiv CH$ + H + O_2 experiment. This feature is a likely candidate for the C=C stretching mode of propenols. This peak does not overlap with infrared signatures in the $H_3CC\equiv CH$ + H, $H_3CC\equiv CH$, n- or i-propanol experiments, meaning it does not represent a product or reactant
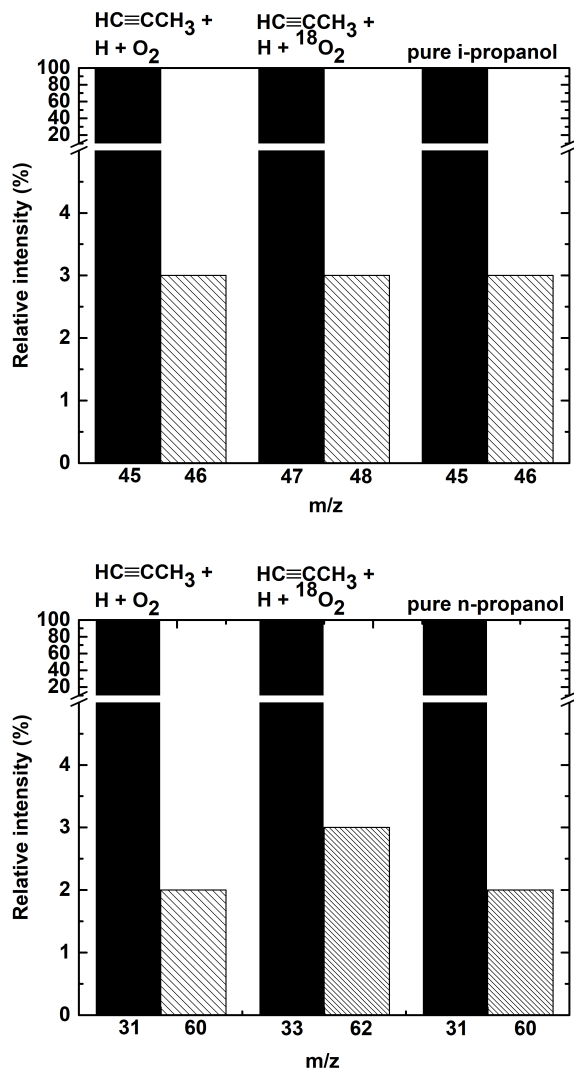
Figure 8.5: QMS fragmentation pattern of two m/z values that are normalized to the QMS signal of the $CHOHCH_3^+$ ion (top) and CH_2OH^+ ion (bottom) found in the $HC{\equiv}CCH_3 + H + O_2$ (exp. 2.0), $HC{\equiv}CCH_3 + H + {}^{18}O_2$ (exp. 2.1), and pure i- and n-propanol experiments (exps. 3.0 and 3.1 respectively) for a temperature of 160 K (top) and 163 K (bottom).

from those experiments. It also does not red-shift in the $H_3CC{\equiv}CH$ + H + $^{18}O_2$ experiment (not shown here), therefore the correlated functional group does not include oxygen. As shown in Shaw et al. (2017), n- and i-propenol have strong absorptions for the C=C stretch at 1684 cm^{-1} and 1678 cm^{-1}, respectively. Our value of 1668 cm^{-1} is expected, as solid-state infrared frequencies can be red-shifted from that of the gas-phase due to the ice matrix (e.g., CO_2) (Isokoski et al. 2013). The C=C stretching mode is also one of the strongest bands of propenol (Shaw et al. 2017), and thus has the highest probability to be visible in our data. The other propenol vibrational modes with relatively high band strengths (i.e., the COH bend at $\sim$ 1100 cm^{-1} and OH stretch at $\sim$ 3600 cm^{-1}) (Shaw et al. 2017) unfortunately overlap with modes of multiple products in the $H_3CC{\equiv}CH$ + H + O_2 experiment. As a direct consequence, an unambiguous identification of propenol in the RAIR data is currently not possible.

For TPD-QMS, since electron impact ionization fragmentation patterns of n- and i-propenol are not available, simple assumptions have to be used to theoretically derive the possible fragment m/z values. With an electron energy of 70 eV, single bonds can easily break upon dissociative ionization. For both propenols, this results in species with m/z pairs of 43 ($C_2H_2OH^+$) and 15 (CH_3^+), and 41 ($C_3H_5^+$) and 17 (OH^+). n- and i-propenol can also remain intact (non-dissociative ionization), which will result in a m/z = 58 signal. Removal of an H-atom from the O/C-atom of propenol results in a signal for m/z = 57. In the $H_3CC{\equiv}CH$ + H + $^{18}O_2$ experiment, these values bump up to 45 and 15; 41 and 19; 60; and 59; respectively. The signals for some of these m/z values are shown in Figure 8.6. Two desorption peaks are displayed with peak desorption temperatures of around $\sim$ 153 and $\sim$ 159 K in the regular and isotopically-enhanced experiments, which is in the range for which the desorption of propenols is expected. From our estimated propenol fragment results, it is not possible to conclude which desorption peak corresponds to which propenol desorption. It should be stressed that no positive identification for the tautomers, propanal and acetone, could be found at their corresponding desorption temperatures of 125 K (Qasim et al. 2019) and 133 K (Schaff & Roberts 1998), respectively. The signal of m/z = 43 from $\sim$ 130 - 170 K has some overlap with the signals of m/z = 57 and 58, and appears to contain other oxygen containing COMs due to its broad and bumpy desorption profile. Like that of n- and i-propanol, the desorption temperatures of tentatively assigned n- and i-propenol are not that far apart. However, the difference in desorption temperature between isomers also varies depending on the isomers involved. The peak desorption temperatures of around $\sim$ 153 and $\sim$ 159 K shown in Figure 8.6 are within the range of n-propenol desorption of 146 - 185 K (Abplanalp et al. 2016), and are also between the peak desorption temperatures of propanal (125 K) (Qasim et al. 2019) and n-propanol (160 K). This is expected when comparing the desorption temperature trend to that of the two-carbon counterparts, acetaldehyde (H_3CCHO), vinyl alcohol (H_2CCHOH), and ethanol (H_3CCH_2OH), which have peak desorption temperatures of 131 K, 146 K, and 164 K, respectively (Chuang et al. in prep). Yet, without mass spectra and information on the desorption temperatures and profiles of pure n- and i-propenol, the formation of both species in the $H_3CC{\equiv}CH$ + H + O_2 experiment can only be concluded as tentative.
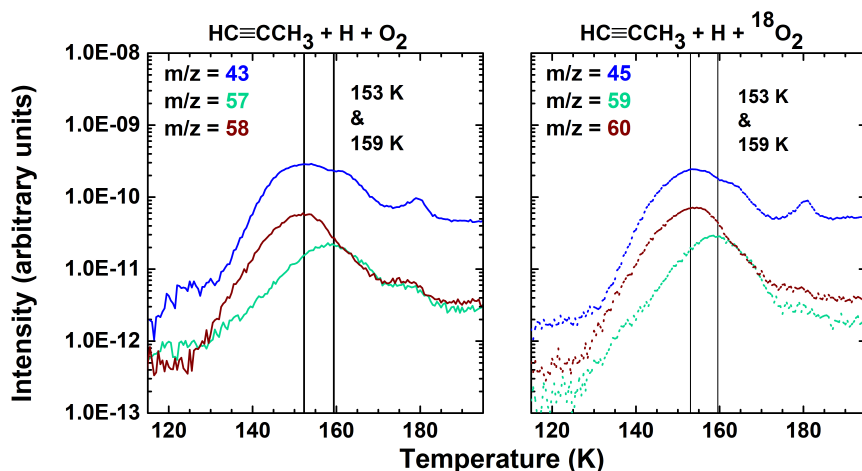
Figure 8.6: TPD-QMS fragment spectra acquired after deposition of HC≡CCH$_3$ + H + O$_2$ (left; exp. 2.2) and HC≡CCH$_3$ + H + ^{18}O$_2$ (right; exp. 2.3) on a 10 K surface. n- and i-propenol are tentatively identified. It cannot be distinguished which of the two propenol isomers desorbs at 153 K and which desorbs at 159 K. The desorption features at ∼ 180 K are due to the co-desorption of both species with H$_2$O$_2$ (an abundant product of H + O$_2$), where both species were trapped in the H$_2$O$_2$ bulk ice.

8.3.2.3 Tentative experimental evidence of the formation of other oxygen-bearing COMs: three isomers of propanediol

The hydroxylation of n- and i-propenol can lead to the formation of COMs with two oxygens, such as propane-1,1-diol, propane-2,2-diol, and propane-1,2-diol. However, study of the pure samples is difficult due to their chemical instability and low vapor pressure under standard temperature and pressure conditions. Particularly, propane-1,1-diol and propane-2,2-diols are very unstable, and are therefore not commercially available. Upon desorption into the gas-phase, the geminal-diol equilibrium of propane-1,1-diol and propane-2,2-diol shifts greatly towards formation of the spontaneous decomposition products, propanal with H$_2$O and acetone with H$_2$O, respectively (Dewick 2006). Such chemical transformations can be used to tag the formation of propanediol isomers. If the geminal diols are formed in the solid-state, then upon their desorption into the gas-phase following spontaneous decomposition, QMS signatures of propanal, acetone, and H$_2$O would be observed at their non-characteristic desorption temperature of around 200 K, where propanal and acetone have characteristic peak desorption temperatures of 125 K (Qasim et al. 2019) and 133 K (Schaff & Roberts 1998), respectively. As shown in Figure 8.7, m/z = 43, 29, 31 and 45 represent the main m/z signals of acetone, propanal, and propane-1,2-diol, respectively, according to the NIST database. The peak intensity of these values is found around ∼ 207 K, which is in-line with the temperature of 203 K that was tentatively assigned for propane-1,2-diol and propane-1,3-diol desorption (Maity et al. 2015). The expected m/z shifts are also found in the H$_3$CC≡CH + H + ^{18}O$_2$ experiment, as shown in the right panel of Figure 8.7. Yet, without confirmation of the desorption temperatures,

decomposition products, and fragmentation patterns of the pure samples, only a tentative identification of the isomers of propanediol is reported here.
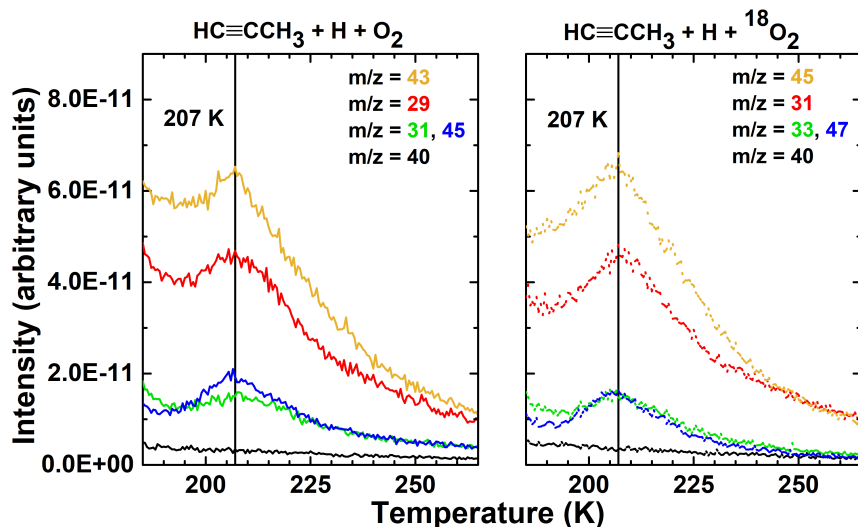
Figure 8.7: TPD-QMS fragment spectra acquired after deposition of $HC\equiv CCH_3$ + H + O_2 (left; exp. 2.2) and $HC\equiv CCH_3$ + H + $^{18}O_2$ (right; exp. 2.3) on a 10 K surface. Tentatively identified peaks of propane-1,1-diol decomposition product (propanal; m/z = 31, 45), propane-2,2-diol decomposition product (acetone; m/z = 43), and propane-1,2-diol (m/z = 31, 45) are shown. "Blank" refers to the m/z value that does not have a peak desorption in the illustrated temperature range.

We summarize all the experimental results presented here. As shown in Section 8.3.1, $H_3CCH=CH_2$ and $H_3CCH_2CH_3$ are experimentally confirmed to form from the hydrogenation of $H_3CC\equiv CH$, with an abundance ratio of $HC\equiv CCH_3$:$H_3CCH=CH_2$:$H_3CCH_2CH_3$ 9:1:2. In Section 8.3.2, it is shown that inclusion of OH leads to the formation of n- and i-propanol, and the average abundance ratio of n-propanol:i-propanol is 1:1. Tentative detections of n- and i-propenol, propane-1,1-diol, propane-2,2-diol, and propane-1,2-diol are found. The tautomers of n-propenol (propanal) and i-propenol (acetone), as well as the acidic derivative propanoic acid, are not detected.

8.4 Energies and formation mechanisms

The experimental findings are joined by computationally derived energy barriers to draw the exact products formed and the correlated formation mechanisms. Computationally derived energies for eight different reactions that occur in the experiments are found in Table 8.4. The first column of the table lists three types of energies studied: interaction, activation, and reaction. The interaction energy is the energy gained when the pre-reactive complex (PRC) is formed. This complex is formed when the two reactants have enough time or energy to rearrange themselves in the ice before product formation. This is

Table 8.4: Interaction, activation, and reaction energies for $H_3CC\equiv CH$ + OH, $H_3CCH=CH_2$ + OH, $H_3CC\equiv CH$ + H, and $H_3CCH=CH_2$ + H calculated at the MPWB1K/def2-TZVP level of theory. E and I refer to the exterior and interior carbon, respectively. SR and PRC refer to the separated reactants and pre-reactive complex, respectively. All values are in units of Kelvin.

Energy type	E or I carbon	SR or PRC	Total
$HC\equiv CCH_3$ + OH			
Activation	I	SR	636
Activation	E	SR	380
Activation	I	PRC	1387
Activation	E	PRC	1762
$H_2C=CHCH_3$ + OH			
Activation	I	SR	-691
Activation	E	SR	-671
Activation	I	PRC	47
Activation	E	PRC	221
$HC\equiv CCH_3$ + H			
Activation	I	SR	2866
Activation	E	SR	1742
Activation	I	PRC	2634
Activation	E	PRC	1591
$H_2C=CHCH_3$ + H			
Activation	I	SR	2136
Activation	E	SR	1109
Activation	I	PRC	1960
Activation	E	PRC	991

opposite to the situation of the separated reactants (SR), where the reactants immediately react to form the end product. The activation energy is with respect to both SR and with respect to the PRC, and the difference between these two values is equal to the interaction energy of the PRC. Finally, the reaction energy is defined by the exothermicity.

The main findings from Table 8.4 are discussed as follows. Comparing the reactivity towards H and OH, in all but one case the reaction of an unsaturated species with an OH radical is more favorable than with an H atom. However, it is important to keep in mind that the reaction with OH results in the formation of a C-O bond. This, contrary to the formation of a C-H bond, is not accelerated much by taking tunneling into account at low temeprature. Furthermore, in accordance with results from Kobayashi et al. (2017) and Zaverkin et al. (2018), we find that reaction with a double-bonded (C=C) species is easier than with a triple-bonded (C≡C) molecule. It is also confirmed that the exterior carbon is more reactive towards H than the interior carbon.

Whether the reactions proceed with or without a PRC is evaluated from the results from Table 8.4. When the activation energies for the reactions, $H_3CC\equiv CH$ + OH and $H_3CCH=CH_2$ + OH (where OH is derived from H + O_2 in the experiments), are considered with respect to the separated reactants, it is obvious that the reactions should be able to take place very easily as the reaction is either barrierless ($H_3CCH=CH_2$ + OH) or has a relatively low activation energy ($H_3CC\equiv CH$ + OH, 380 or 636 K). However, when the two reactants form a PRC, it is expected that the excess energy of the complex formation is dissipated into the ice mantle well before the reaction itself is attempted, as the energy dissipation in ices seems to take place on a picosecond timescale (Arasa et al. 2010; Fredon et al. 2017). Therefore, the effective activation energy to be overcome increases by the same amount of energy that is gained from the interaction of OH with $H_3CC\equiv CH/H_3CCH=CH_2$ (i.e., the interaction energy is added to determine the total activation energy). This significantly increases the activation energy, although for the reaction with $H_3CCH=CH_2$, it remains close to barrierless. Which of the two surface 'mechanisms' is the best description for these reactions in an ice (be it in the laboratory or in the interstellar medium) can be debated and it is quite likely that a variety of geometries exist that may lead to an averaged-out effect. For example, if OH is a neighboring species to $H_3CC\equiv CH/H_3CCH=CH_2$, the immediate surroundings may cause steric hindrance between the two species, and therefore mitigate a favorable orientation of the two species with respect to each other. On the other hand, OH could potentially use its excess energy to rearrange the position and thus obtain a more favorable orientation. Note that for the reaction of H with any molecule, the low diffusion barrier of the H-atom always allows for a mechanism that considers the PRC to take place. Therefore, the effect of the relative geometries on the reaction efficiency is less pronounced for species that have low diffusion barriers or high activation barriers.

The likelihood of constitutional isomerization (or tautomerization) for products formed in the experiments is assessed from the computationally-derived results in Table 8.5. From the results, it is immediately clear that direct isomerization reactions cannot take place efficiently in ices in cold interstellar clouds, as the typical activation energy is more than 25,000 K. If the reaction were to be actively catalyzed by another molecule that can simultaneously donate and accept an H-atom, such as H_2O or the OH-group of CH_3OH, the activation energy may drop considerably (Vöhringer-Martinez et al. 2007; Rimola et al. 2018). The value could then drop close to the values involved for H-hopping from an OH group to an OH radical, which is > 1800 K for the reaction CH_3OH + OH (Xu & Lin 2007), and between 2500 - 9000 K for the reaction OH + $(H_2O)_n$ (n = 1-3) (Gonzalez et al. 2011). This can only happen, however, if a suitable multi-species geometry can be established in the ice (i.e., if solvation is present).

The products formed and their formation mechanisms are finally discussed below. It is apparent from Table 8.4 that the activation barriers of $H_3CC\equiv CH$ + OH are primarily lower than that of $H_3CC\equiv CH$ + H and by a substantial amount. This is even more pronounced when comparing the activation barriers of $H_3CCH=CH_2$ + OH and $H_3CCH=CH_2$ + H. The formation of propanols in the experiments indicates that OH-addition is relatively efficient under our experimental conditions. However, H-atoms are more mobile and can effectively

Table 8.5: Activation barriers of the isomerization reactions of n- and i-propenol. All values are in units of Kelvin.

Reaction	PES	ZPE	Total
Acetone $\rightarrow$ i-propenol	34452	-1692	32760
i-propenol $\rightarrow$ acetone	28686	-2116	26569
Propanal $\rightarrow$ n-propenol	35132	-1892	33240
n-propenol $\rightarrow$ propanal	31209	-2100	29109

tunnel at low temperatures, making H-addition competitive to OH-addition. Therefore, from the combination of computationally-derived activation barriers and the unambiguous identification of propanol formation, it is found that $H_3CC\equiv CH$ is effectively attacked by OH radicals more so than by H-atoms only when both species neighbor $H_3CC\equiv CH$, and when OH is oriented in a favorable position for reaction. According to Table 8.4, this narrows the selection of activation energies to four values: 636 and 1387 K (OH attack on the interior carbon) and 380 and 1762 K (OH attack on the exterior carbon). The experimental results give an n-propanol:i-propanol average abundance ratio of 1:1, depending on which m/z values are used to determine the relative abundance. Therefore, it is likely that both species are formed with comparable abundances (i.e., attack to the exterior and interior carbons occurs equally under our experimental conditions). Moreover, this conclusion is fully in-line with the idea that for reactants that can strongly interact with each other, the efficiency of both 'mechanisms' is influenced by the geometric orientation of the formed OH radical with respect to the $H_3CC\equiv CH$ molecule (i.e., both 'mechanisms' are actively participating). If this was not the case, then it is expected that n-propanol would be distinctly more abundant in the experiments, as the lowest activation barrier of 380 K would favor n-propanol formation. The outcome of the experimental and theoretical results pieced together leads to the formation mechanisms that are most likely occurring in the $H_3CC\equiv CH$ + H + O_2 experiment, which are illustrated in Figure 8.8. The activation barriers for some of the displayed reaction steps are listed in Table 8.4. As shown, the formation pathways of n- and i-propanol include the formation of n- and i-propenol. Thus, n- and i-propenol are products formed in our experiments. Since the activation barriers of OH-addition to propenols are not investigated in this work, the propanediol isomers remain to be tentative reaction products, as noted in Figure 8.8. For the $H_3CC\equiv CH$ + H experiment, the relatively high barriers show that $H_3CC\equiv CH$ and H do not have a strong interaction with each other as that of $H_3CC\equiv CH$ and OH. Therefore, the geometric orientation of the two species has less of an effect on which 'mechanism' would proceed. H-attack on the exterior carbon of $H_3CC\equiv CH$ and $H_3CCH=CH_2$ results in the lower activation barrier in comparison to H-attack on the interior carbon, and thus is proposed to be the more likely scenario involved in $H_3CCH=CH_2$ and $H_3CCH_2CH_3$ formation.

Formation of propene ($H_2C=CHCH_3$) and propane ($H_3CCH_2CH_3$)

$H_3CC{\equiv}CH$
↓ H
$H_3CC=CH_2$
↓ H
$\boxed{H_3CCH=CH_2}$
↓ H
H_3CCHCH_3
↓ H
$\boxed{H_3CCH_2CH_3}$

Formation of n-propenol ($H_3CCH=CHOH$) and n-propanol ($H_3CCH_2CH_2OH$)

$H_3CC{\equiv}CH$
↓ OH
$H_3CC=CHOH$
↓ H
$\boxed{H_3CCH=CHOH}$
↓ H
$H_3CCHCH_2OH/$
H_3CCH_2CHOH
↓ H
$\boxed{H_3CCH_2CH_2OH}$

Formation of i-propenol ($H_3CCOH=CH_2$) and i-propanol ($H_3CCHOHCH_3$)

$H_3CC{\equiv}CH$
↓ OH
$H_3CCOH=CH$
↓ H
$\boxed{H_3CCOH=CH_2}$
↓ H
$H_3CCHOHCH_2/$
$H_3CCOHCH_3$
↓ H
$\boxed{H_3CCHOHCH_3}$

Formation of propane-1,1-diol ($H_3CCH_2CH(OH)_2$), propane-2,2-diol ($H_3CC(OH)_2CH_3$), and propane-1,2-diol ($H_3CCHOHCH_2OH$)

$H_3CC{\equiv}CH$
↓ OH
$H_3CC=CHOH/H_3CCOH=CH$
↓ H
$\boxed{H_3CCH=CHOH/H_3CCOH=CH_2}$
↓ OH   ↓ OH
$H_3CCHCH(OH)_2/$ $H_3CC(OH)_2CH_2/$
$H_3CCHOHCHOH$ $H_3CCOHCH_2OH$
↓ H   ↓ H

$H_3CCH_2CH(OH)_2/$ $H_3CC(OH)_2CH_3/$
$H_3CCHOHCH_2OH$ $H_3CCHOHCH_2OH$

Figure 8.8: Proposed mechanisms for exps. 2.0 and 2.2. Relevant species within each mechanism are boxed. Species labeled with green font are those that have been detected in space. Dotted-boxes indicate tentatively identified species in this study.

8.5 Astrochemical and astrobiological implications

The formation of three-carbon chains, alcohols, and to an extent, geminal diols, from $H_3CC{\equiv}CH$ + H/OH at the low temperature of 10 K can take place at the interface of carbonaceous grains and H_2O-rich ice in the cold cloud stage of stellar formation. At an $A_V < 1.5$, H_2O is just starting to coat interstellar grains partially by the accretion of H and O atoms (Boogert et al. 2015). These atoms combine on the grain surface to form OH radicals and have the potential to react with the carbon-rich constituents that are at the surface of the dust grain. As the visual extinction grows to 3, a H_2O-rich ice is formed on top of the mineral-ice interface. The icy grain is further coated by other molecules (e.g., CO) as it travels through various molecular freeze-out stages (Boogert et al. 2015).

The formation of n- and i-propanol and propenol shown in this combined experimental and theoretical study brings to light possible formation pathways for these species in astrochemical environments. Particularly, the formation of solid-state i-propanol and propenol is intriguing, as there are no experimentally-based studies on these molecules to our knowledge. It has been shown by Qasim et al. (2019) and Abplanalp et al. (2016) that n-propanol and propenol can be formed in a CO-rich ice, respectively. For the first time experimentally, it is shown here that all four alcohols can be formed before the heavy CO freeze-out stage (i.e., in the H_2O-rich ice phase) and along the same formation route. Thus, astronomical surveys may be able to identify all four species simultaneously.

This route can be extrapolated to polyynes containing H_3C-$(C{\equiv}C)_n$-H structures and therefore have an astrobiological context. As a $H_3CC{\equiv}CH$-containing ice yields n-propanol, similarly ices with H_3C-$(C{\equiv}C)_n$-H structures can lead to the formation of fatty alcohols (i.e., long-chain alcohols), which are found to

be constituents of simple lipids. For example, the incorporation of dodecanol to form primitive-like lipid bilayer membranes has been shown (Hargreaves & Deamer 1978). Moreover waxes, which are simple lipids, are composed of fatty alcohols which fatty acids are attached to. This includes the wax spermaceti, which contains hexadecan-1-ol ($H_3C(CH_2)_{14}CH_2OH$), and beeswax and carnuba, which both contain triacontan-1-ol ($H_3C(CH_2)_{28}CH_2OH$) (Alamgir 2018).

The hydroxylation of polyynes discussed in our study provides a valid mechanism for the formation of various linear alcohols starting from carbon chains. Such alcohols maybe present in the bottom layer (layer closest to the grain surface) of H_2O-rich interstellar ices. Such layering is advantageous to the preservation of such interface reaction products, in that bulk H_2O-ice can partially block UV-light (Gerakines et al. 2000; Cottin et al. 2003). From there, the possibility increases for such prebiotic material to be safely transferred to the early Earth and contribute to the formation of primitive cell membranes.

8.6 Conclusions

This combined experimental and computational study provides insights into what and how solid-state alcohols may be formed in the H_2O-rich ice phase of cold molecular cores. The main conclusions from the conjoined results are highlighted below:

◆ $H_3CC\equiv CH$ (propyne) + H forms $H_3CCH=CH_2$ (propene) and $H_3CCH_2CH_3$ (propane) efficiently, where the abundance ratio of the three species is 9:1:2, respectively. The experimental result is in-line with the computational results, in that the barrier to hydrogenate C=C is lower than to hydrogenate C≡C.

◆ The experimental investigation shows that $H_3CC\equiv CH$ + OH leads to the formation of n- and i-propanol at 10 K under 'non-energetic' (without UV, cosmic rays, etc. and/or other 'energetic' particles) conditions. The formation of n- and i-propenol in our experiments is confirmed from the combination of the experimental and theoretical results. Tentative identifications of propane-1,1-diol, propane-2,2-diol, and propane-1,2-diol are found from the experimental data.

◆ The formation yield of n-propanol (and thus n-propenol) in the experiments is observed to be comparable to that of i-propanol (and thus i-propenol), with an experimentally-measured n-propanol:i-propanol average abundance ratio of 1:1. This value is in-line with the computational calculations and the finding that both 'mechanisms' (PRC and SR) are equally influential due to the prominent role of how $H_3CC\equiv CH$ and OH are oriented towards each other.

◆ OH-addition to $H_3CC\equiv CH$ is observed to be more effective than H-addition when both radicals are in close vicinity to $H_3CC\equiv CH$, and when the OH radical is situated in a favorable orientation for reaction. This is supported by the relatively low computationally-derived activation barriers of $H_3CC\equiv CH$ + OH and the formation of propanols in the experiments.

◆ Propanols and propenols, and to an extent propanediols, are expected to form simultaneously in suitable ISM regions and may have an icy origin at the very beginning of interstellar clouds.

◆ The presented formation routes may be extended to polyynes with H_3C-$(C{\equiv}C)_n$-H structures. These structures can transform into fatty alcohols, which are the components of simple lipids which primitive cell membranes, were likely, in part, assembled by.

S1 Additional TPD-QMS spectra
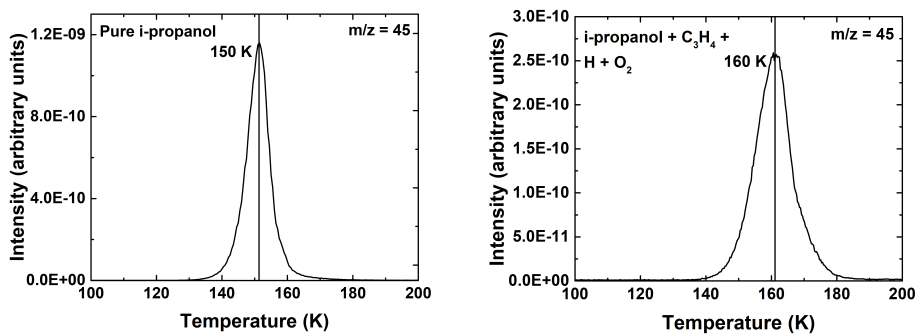
Figure S1: TPD-QMS fragment spectra acquired after deposition of i-propanol (top; exp. 3.1) and i-propanol + H + O$_2$ (bottom; exp. 3.2) on a 10 K surface. Note the 10 K shift of the main desorption peak of i-propanol between the two experiments.

S2 Pathways and benchmark calculations

S2.1 IRC paths

For the reaction $H_3CC{\equiv}CH$ + OH, we perform IRC calculations to confirm that the found transition state structures connect the relevant pre-reactive complex and desired product. The resulting paths are presented in Figures S2 and S3. The pre-reactive complex energy is set to zero, acting as the reference value for the energy.

Examining Figure S3, it also becomes clear why the activation energy for the reaction $H_3CC{\equiv}CH$ + OH on the exterior carbon atom has such a high activation energy in comparison to that at the center carbon. This is because there is an extra rotation of the OH radical involved in order to reach the transition state structure. In other words, this only plays a role for a starting geometry where the OH and $H_3CC{\equiv}CH$ are fully relaxed.
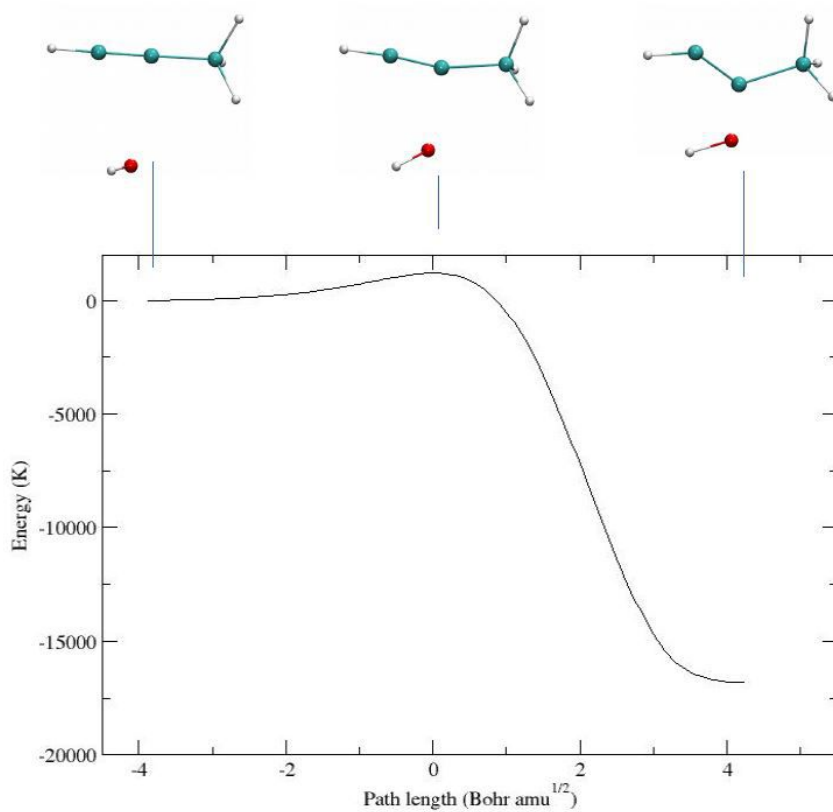
Figure S2: Intrinsic reaction coordinate path for the reaction $H_3CC\equiv CH$ + OH on the centered carbon atom. The geometries corresponding to the pre-reactive complex, transition state, and product are displayed above.
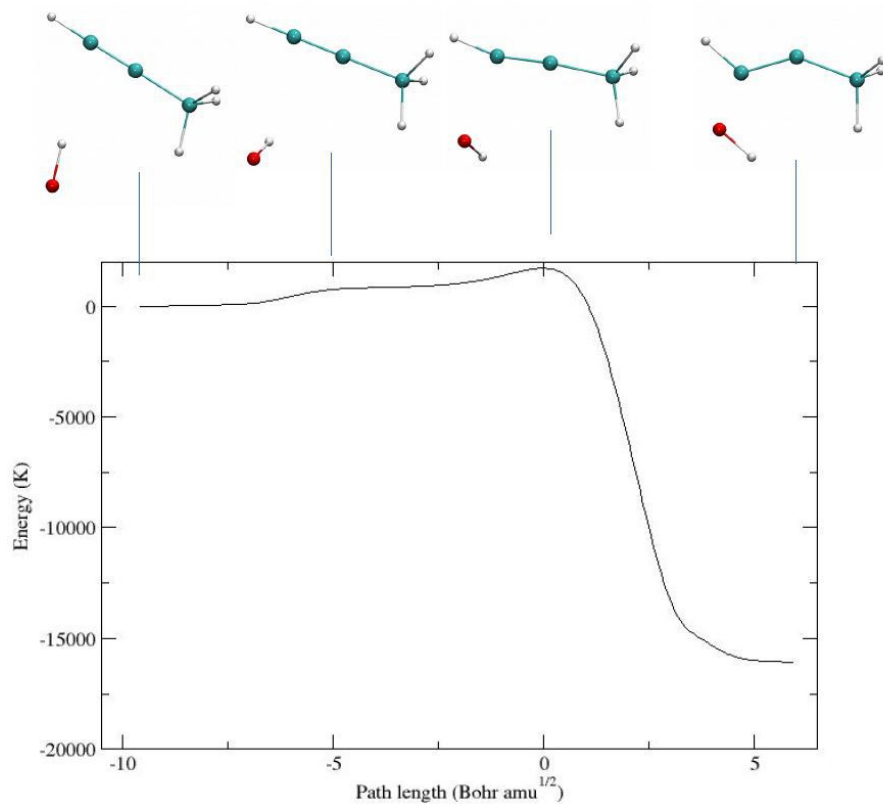
Figure S3: Intrinsic reaction coordinate path for the reaction H$_3$CC≡CH + OH on the exterior carbon atom. The geometries corresponding to the pre-reactive complex, an intermediate state, the transition state, and product are displayed above.

S2.2 NEB paths
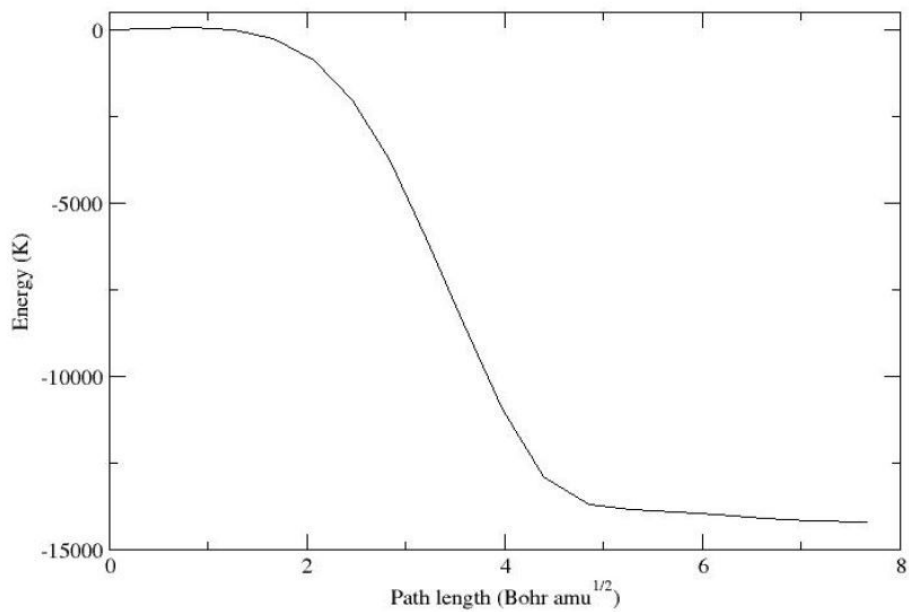
Figure S4: Nudged-elastic band path for the reaction $H_3CCH=CH_2$ + OH on the centered carbon atom.
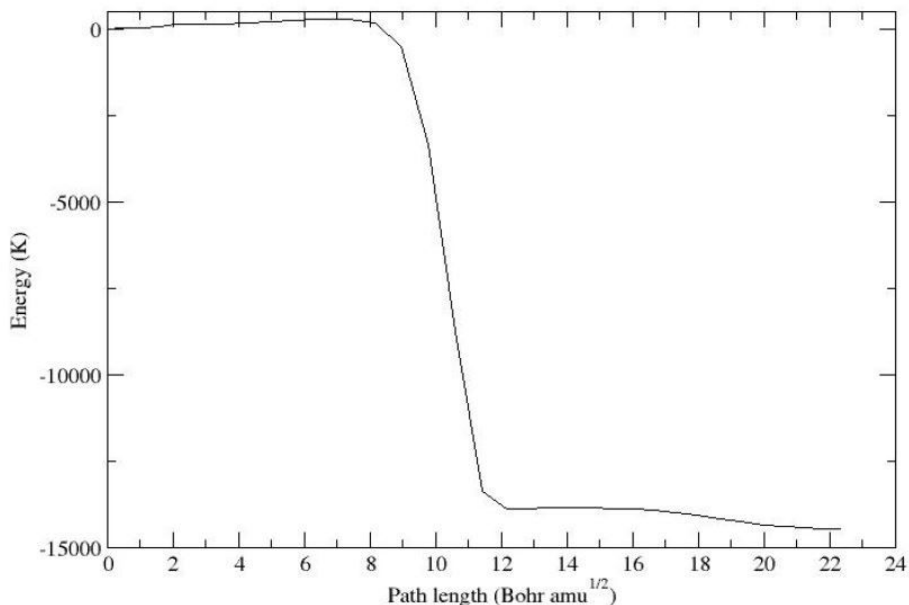
Figure S5: Nudged-elastic band path for the reaction H$_3$CCH=CH$_2$ + OH on the exterior carbon atom.

S2.3 M06-2X validity check

In order to test if the use of the MPWB1K is valid, the activation energies have been recalculated with the M06-2X functional with the same basis set (def2-TZVP). This is a functional very commonly used for these types of reactions as well and is thought to be able to reasonably describe the reaction paths. Indeed, it is shown in Table S1 that the activation energies that are responsible for determining the reactivity differ by at most 240 K, indicating a proper choice of functional.

Table S1: Reaction of $H_3CC\equiv CH + OH$ and $H_3CCH=CH_2 + OH$, respectively. E and I refer to the exterior and interior carbon, respectively. All values are in units of Kelvin.

| | | $HC\equiv CCH_3 + OH$ | | |
| | | MPWB1K | | |
Energy type	E or I carbon	PES	ZPE	Total
Activation	I	-126	763	636
Activation	E	-358	738	380
Reaction	I	-16928	2089	-14839
Reaction	E	-18122	2333	-15790
		M06-2X		
Energy type	E or I carbon	PES	ZPE	Total
Activation	I	-59	773	714
Activation	E	-110	729	619
Reaction	I	-17224	2054	-15170
Reaction	E	-18006	2296	-15710
		$H_2C=CHCH_3 + OH$		
		MPWB1K		
Energy type	E or I carbon	PES	ZPE	Total
Activation	I	-1490	799	-691
Activation	E	-1358	687	-671
Reaction	I	-15736	1692	-14045
Reaction	E	-16088	1825	-14263
		M06-2X		
Energy type	E or I carbon	PES	ZPE	Total
Activation	I	-1557	837	-720
Activation	E	-1420	775	-645
Reaction	I	-11299	2160	-9139
Reaction	E	-16772	1901	-14871

S2.4 CCSD(T)-F12/cc-VDZ-F12 validity check

As a further validity check, the interaction energies of the OH-C_3H_n pre-reactive complexes calculated with MPWB1K (DFT) are compared to those calculated with CCSD(T)-F12/cc-VDZ-F12. The interaction energies of the OH-C_3H_n pre-reactive complexes differ by at most 115 K between MPWB1K and CCSD(T)-F12/cc-VDZ-F12 calculations, as shown in Table S2. This shows again that the used functional can accurately describe these reaction paths. For the pre-reactive complex of OH with $H_3CC\equiv CH$ on the exterior carbon atom, convergence is not achieved for the CCSD(T)-F12/cc-VDZ-F12 calculation.

Table S2: Interaction energies of OH with $H_3CC\equiv CH$ and $H_3CCH=CH_2$. E and I refer to the exterior and interior carbon, respectively. All values are in units of Kelvin.

$HC\equiv CCH_3$ + OH		
E or I carbon	PES MPWB1K	PES CCSD(T)-F12/cc-VDZ-F12
I	-1342	-1333
E	-2073	-
$H_3CCH=CH_2$ + OH		
E or I carbon	PES MPWB1K	PES CCSD(T)-F12/cc-VDZ-F12
I	-1543	-1509
E	-1624	-1510

Bibliography

Abplanalp, M. J., Góbi, S., & Kaiser, R. I. 2018, Phys. Chem. Chem. Phys., 21, 5378

Abplanalp, M. J., Gozem, S., Krylov, A. I., et al. 2016, Proc. Natl. Acad. Sci. U.S.A., 113, 7727

Adler, T. B., Knizia, G., & Werner, H.-J. 2007, J. Chem. Phys., 127, 1

Agúndez, M., Fonfría, J. P., Cernicharo, J., Pardo, J., & Guélin, M. 2008, Astron. Astrophys., 479, 493

Alamgir, A. 2018, Therapeutic use of medicinal plants and their extracts: volume 2: phytochemistry and bioactive compounds, Vol. 74 (Cham, Switzerland: Springer)

Arasa, C., Andersson, S., Cuppen, H., van Dishoeck, E. F., & Kroes, G.-J. 2010, J. Chem. Phys., 132, 1

Ball, J. A., Gottlieb, C. A., Lilley, A., & Radford, H. 1970, Astrophys. J., 162, L203

Bernstein, M. P., Sandford, S. A., Allamandola, L. J., Chang, S., & Scharberg, M. A. 1995, Astrophys. J., 454, 327

Boogert, A., Gerakines, P. A., & Whittet, D. C. 2015, Annu. Rev. Astron. Astrophys., 53, 541

Boogert, A., Huard, T., Cook, A., et al. 2011, Astrophys. J., 729, 1

Budin, I. & Szostak, J. W. 2011, Proc. Natl. Acad. Sci. U.S.A., 108, 5249

Burdett, J. L. & Rogers, M. T. 1966, J. Phys. Chem., 70, 939

Butscher, T., Duvernay, F., Rimola, A., Segado-Centellas, M., & Chiavassa, T. 2017, Phys. Chem. Chem. Phys., 19, 2857

Butscher, T., Duvernay, F., Theule, P., et al. 2015, Mon. Not. R. Astron. Soc., 453, 1587

Castellanos, N. P. 2018, PhD thesis

Cernicharo, J., Heras, A. M., Pardo, J. R., et al. 2001, Astrophys. J. Lett., 546, L127

Chang, Q. & Herbst, E. 2012, Astrophys. J., 759, 1

Chen, Y.-J., Ciaravella, A., Caro, G. M., et al. 2013, Astrophys. J., 778, 1

Cherchneff, I. 2011, EAS Publications Series, 46, 177

Chuang, K. 2018, Univ. Leiden, PhD thesis

Chuang, K.-J., Fedoseev, G., Ioppolo, S., van Dishoeck, E. F., & Linnartz, H. 2016, Mon. Not. R. Astron. Soc., 455, 1702

Chuang, K.-J., Fedoseev, G., Qasim, D., et al. 2018, Astron. Astrophys., 617, 1

Chyba, C. F., Thomas, P. J., Brookshaw, L., & Sagan, C. 1990, Science, 249, 366

Collings, M. P., Anderson, M. A., Chen, R., et al. 2004, Mon. Not. R. Astron. Soc., 354, 1133

Comeford, J. & Gould, J. H. 1961, J. Mol. Spectrosc., 5, 474

Contreras, C. S. & Salama, F. 2013, Astrophys. J. Suppl. Ser., 208, 1

Cottin, H., Moore, M. H., & Bénilan, Y. 2003, Astrophys. J., 590, 874

Cuppen, H. & Herbst, E. 2007, Astrophys. J., 668, 294

Cuppen, H., Ioppolo, S., Romanzin, C., & Linnartz, H. 2010, Phys. Chem. Chem. Phys., 12, 12077

Cuylle, S. H., Zhao, D., Strazzulla, G., & Linnartz, H. 2014, Astron. Astrophys., 570, 1

De Rosa, M., Gambacorta, A., & Gliozzi, A. 1986, Microbiol. Rev., 50, 70

Deamer, D., Dworkin, J. P., Sandford, S. A., Bernstein, M. P., & Allamandola, L. J. 2002, Astrobiology, 2, 371

Deegan, M. J. & Knowles, P. J. 1994, Chem. Phys. Lett., 227, 321

Dewick, P. M. 2006, Essentials of organic chemistry: for students of pharmacy, medicinal chemistry and biological chemistry (New York: John Wiley & Sons)

Fedoseev, G., Cuppen, H. M., Ioppolo, S., Lamberts, T., & Linnartz, H. 2015, Mon. Not. R. Astron. Soc., 448, 1288

Fredon, A., Lamberts, T., & Cuppen, H. 2017, Astrophys. J., 849, 1

Fuchs, G., Cuppen, H., Ioppolo, S., et al. 2009, Astron. Astrophys., 505, 629

Gerakines, P., Moore, M. H., & Hudson, R. L. 2000, Astron. Astrophys., 357, 793

Ghosh, J., Hariharan, A. K., Bhuin, R. G., Methikkalam, R. R. J., & Pradeep, T. 2018, Phys. Chem. Chem. Phys., 20, 1838

Gonzalez, J., Caballero, M., Aguilar-Mogas, A., et al. 2011, Theor. Chem. Acc., 128, 579

Hama, T. & Watanabe, N. 2013, Chem. Rev., 113, 8783

Hargreaves, W. R. & Deamer, D. W. 1978, Biochemistry, 17, 3759

Herbst, E. & van Dishoeck, E. F. 2009, Annu. Rev. Astron. Astrophys., 47, 427

Hollis, J. M., Lovas, F. J., Jewell, P. R., & Coudert, L. 2002, Astrophys. J. Lett., 571, L59

Hratchian, H. P. & Schlegel, H. B. 2004, J. Chem. Phys., 120, 9918

Ioppolo, S., Cuppen, H., Romanzin, C., van Dishoeck, E. F., & Linnartz, H. 2008, Astrophys. J., 686, 1474

Ioppolo, S., Cuppen, H., Romanzin, C., van Dishoeck, E. F., & Linnartz, H. 2010, Phys. Chem. Chem. Phys., 12, 12065

Ioppolo, S., Fedoseev, G., Lamberts, T., Romanzin, C., & Linnartz, H. 2013, Rev. Sci. Instrum., 84, 1

Ioppolo, S., Öberg, K., & Linnartz, H. 2014, in Laboratory astrochemistry: from molecules through nanoparticles to grains, ed. S. Schlemmer, T. Giesen, & H. Mutschke (John Wiley & Sons), 289–309

Irvine, W., Hoglund, B., Friberg, P., Askne, J., & Ellder, J. 1981, Astrophys. J., 248, L113

Isokoski, K., Poteet, C., & Linnartz, H. 2013, Astron. Astrophys., 555, 1

Kaifu, N., Ohishi, M., Kawaguchi, K., et al. 2004, Publ. Astron. Soc. Jpn., 56, 69

Kästner, J., Carr, J. M., Keal, T. W., et al. 2009, J. Phys. Chem. A, 113, 11856

Knizia, G., Adler, T. B., & Werner, H.-J. 2009, J. Chem. Phys., 130, 1

Knowles, P. J., Hampel, C., & Werner, H.-J. 1993, J. Chem. Phys., 99, 5219

Knowles, P. J., Hampel, C., & Werner, H.-J. 2000, J. Chem. Phys., 112, 3106

Kobayashi, H., Hidaka, H., Lamberts, T., et al. 2017, Astrophys. J., 837, 1

Kolasinski, K. W. 2012, Surface science: foundations of catalysis and nanoscience (West Chester, PA: John Wiley & Sons)

Kuiper, T., Kuiper, E. R., Dickinson, D. F., Turner, B., & Zuckerman, B. 1984, Astrophys. J., 276, 211

Maity, S., Kaiser, R. I., & Jones, B. M. 2015, Phys. Chem. Chem. Phys., 17, 3081

Malek, S. E., Cami, J., & Bernard-Salas, J. 2011, Astrophys. J., 744, 1

Martín-Doménech, R., Manzano-Santamaría, J., Caro, G. M., et al. 2015, Astron. Astrophys., 584, 1

Matar, E., Congiu, E., Dulieu, F., Momeni, A., & Lemaire, J. 2008, Astron. Astrophys., 492, L17

McGuire, B. A., Shingledecker, C. N., Willis, E. R., et al. 2017, Astrophys. J. Lett., 851, 1

Meisner, J., Markmeyer, M. N., Bohner, M. U., & Kaestner, J. 2017, Phys. Chem. Chem. Phys., 19, 23085

Metz, S., Kästner, J., Sokol, A. A., Keal, T. W., & Sherwood, P. 2014, Wiley Interdiscip. Rev. Comput. Mol. Sci., 4, 101

Miyauchi, N., Hidaka, H., Chigai, T., et al. 2008, Chem. Phys. Lett., 456, 27

Moran, L. A., Horton, H. R., Scrimgeour, G., & Perry, M. 2012, Principles of biochemistry (Upper Saddle River, NJ: Pearson Boston)

Muller, S., Beelen, A., Guélin, M., et al. 2011, Astron. Astrophys., 535, 1

Nykänen, L. & Honkala, K. 2011, J. Phys. Chem. C, 115, 9578

Paardekooper, D., Bossa, J.-B., & Linnartz, H. 2016, Astron. Astrophys., 592, 1

Pascoli, G. & Polleux, A. 2000, Astron. Astrophys., 359, 799

Peterson, K. A., Adler, T. B., & Werner, H.-J. 2008, J. Chem. Phys., 128, 01

Qasim, D., Chuang, K.-J., Fedoseev, G., et al. 2018, Astron. Astrophys., 612, 1

Qasim, D., Fedoseev, G., Chuang, K.-J., et al. 2019, Astron. Astrophys., 627, A1

Qiu, J., Wang, J., Shi, Y., et al. 2018, Astron. Astrophys., 613, 1

Rimola, A., Skouteris, D., Balucani, N., et al. 2018, ACS Earth Space Chem., 2, 720

Romanzin, C., Ioppolo, S., Cuppen, H., van Dishoeck, E. F., & Linnartz, H. 2011, J. Chem. Phys., 134, 1

Schaff, J. E. & Roberts, J. T. 1998, Langmuir, 14, 1478

Shaw, M. F., Osborn, D. L., Jordan, M. J., & Kable, S. H. 2017, J. Phys. Chem. A, 121, 3679

Sherwood, P., de Vries, A. H., Guest, M. F., et al. 2003, J. Mol. Struct.: THEOCHEM, 632, 1

Smith, R. S., May, R. A., & Kay, B. D. 2015, J. Phys. Chem. B, 120, 1979

Snyder, L. & Buhl, D. 1973, Nat. Phys. Sci., 243, 45

Tielens, A. 2013, Rev. Mod. Phys., 85, 1021

Tschersich, K. 2000, J. Appl. Phys., 87, 2565

Tschersich, K., Fleischhauer, J., & Schuler, H. 2008, J. Appl. Phys., 104, 1

Tschersich, K. & Von Bonin, V. 1998, J. Appl. Phys., 84, 4065

Turner, B. E. & Apponi, A. J. 2001, Astrophys. J. Lett., 561, L207

Valiev, M., Bylaska, E. J., Govind, N., et al. 2010, Comput. Phys. Commun., 181, 1477

van Dishoeck, E. F., Herbst, E., & Neufeld, D. A. 2013, Chem. Rev., 113, 9043

van´t Hoff, M. L., Tobin, J. J., Trapman, L., et al. 2018, Astrophys. J. Lett., 864, L23

Vöhringer-Martinez, E., Hansmann, B., Hernandez, H., et al. 2007, Science, 315, 497

Watanabe, N. & Kouchi, A. 2002, Astrophys. J. Lett., 571, L173

Watanabe, N., Shiraki, T., & Kouchi, A. 2003, Astrophys. J. Lett., 588, L121

Weigend, F., Häser, M., Patzelt, H., & Ahlrichs, R. 1998, Chem. Phys. Lett., 294, 143

Werner, H., Knowles, P., Knizia, G., Manby, F., & Schütz, M. 2012, Mol. Sci., 2, 242

Woods, P. M., Millar, T. J., Herbst, E., & Zijlstra, A. A. 2003, Astron. Astrophys., 402, 189

Xu, S. & Lin, M. 2007, Proc. Combust. Inst., 31, 159

Zaverkin, V., Lamberts, T., Markmeyer, M., & Kästner, J. 2018, Astron. Astrophys., 617, 1

Zhao, Y. & Truhlar, D. G. 2004, J. Phys. Chem. A, 108, 6908

Zhao, Y. & Truhlar, D. G. 2008, Theor. Chem. Acc., 120, 215

Zuckerman, B., Turner, B., Johnson, D., et al. 1975, Astrophys. J., 196, L99